Superconductivity in trilayer nickelate $La_4Ni_3O_{10}$ single crystals

Yinghao Zhu[1,2†], Enkang Zhang[1†], Bingying Pan[1,3†], Xu Chen[4†], Di Peng[5†], Lixing Chen[1], Huifen Ren[4], Feiyang Liu[1], Nana Li[5], Zhenfang Xing[5], Jiyuan Han[1], Junjie Wang[4,6], Donghan Jia[7], Hongliang Wo[1], Yiqing Gu[1], Yimeng Gu[1], Li Ji[8], Wenbin Wang[9], Huiyang Gou[7], Yao Shen[4], Tianping Ying[4], Xiaolong Chen[4],Wenge Yang[5], Changlin Zheng[1], Qiaoshi Zeng[5,10*], Jian-gang Guo[4*] & Jun Zhao[1,9,2*]

[1]*State Key Laboratory of Surface Physics and Department of Physics, Fudan University, Shanghai 200433, China*

[2]*Shanghai Research Center for Quantum Sciences, Shanghai 201315, China*

[3]*College of Physics and Optoelectronic Engineering, Ocean University of China, Qingdao, Shandong 266100, China*

[4]*Beijing National Laboratory for Condensed Matter Physics, Institute of Physics, Chinese Academy of Sciences, Beijing 100190, China*

[5]*Center for High Pressure Science and Technology Advanced Research, Shanghai 201203, China*

[6]*School of Physical Sciences, University of Chinese Academy of Sciences, Beijing 100049, China*

[7]*Center for High Pressure Science and Technology Advanced Research, Beijing 100094, China*

[8]*State Key Laboratory of ASIC and System, School of Microelectronics, Fudan University, Shanghai, China.*

[9]*Institute of Nanoelectronics and Quantum Computing, Fudan University, Shanghai 200433, China*

[10] *Shanghai Key Laboratory of Material Frontiers Research in Extreme Environments (MFree), Shanghai Advanced Research in Physical Sciences (SHARPS), Shanghai 201203, China*

Abstract

The pursuit of discovering new high-temperature superconductors that diverge from the copper-based paradigm carries profound implications for elucidating mechanisms behind superconductivity and may also enable new applications.

Here, our investigation reveals that application of pressure effectively suppresses the spin and charge order in trilayer nickelate $La_4Ni_3O_{10}$ single crystals, leading to the emergence of superconductivity with a maximum critical temperature (T_c) of around 30 K. In the normal state, we observe a "strange metal" behavior, characterized by a linear temperature-dependent resistance extending up to 300 K. These results could be interpreted as the pressure's influence, inducing damping on the density-wave gap and spin order, while promoting spin fluctuations and bringing the associated flat d_{z^2} band into close proximity with the Fermi surface. This, in turn, fosters strong correlations and "strange metal" behavior, thus setting the stage for the eventual emergence of superconductivity. Furthermore, the layer-dependent superconductivity observed hints at a unique interlayer coupling mechanism specific to nickelates, setting them apart from cuprates in this regard. Our findings provide crucial insights into the fundamental mechanisms underpinning superconductivity, while also introducing a new material platform to explore the intricate interplay between the spin/charge order, flat band structures, interlayer coupling, strange metal behavior and high-temperature superconductivity.

Cuprates are the first family of high-temperature (high-T_c) superconducting materials, characterized by layers of CuO_2 interleaved with charge reservoir layers[1,2]. Despite intensive research on various cuprates, the mechanism responsible for high-temperature superconductivity remains elusive[2,3]. Consequently, the pursuit of high-temperature superconductors that do not rely on copper oxides has become a focal point of intense experimental and theoretical exploration since the discovery of cuprates nearly four decades ago[4-8]. This is motivated by the belief that such materials may help to elucidate

the enigmatic mechanisms governing high-temperature superconductivity while opening doors to new applications. Nickel, situated immediately to the left of copper on the Periodic Table, offers a playground for materials and chemistry designs aimed at replicating high-temperature unconventional superconductivity[8-12]. However, despite intensive efforts, achieving superconductivity in nickelates has proven to be a formidable challenge. In 2019, an intriguing development occurred when superconductivity was observed in "infinite-layer" nickelate thin films with T_c = 5-15 K[13-16]. In these materials, Ni^{1+} (d^9) forms square planar NiO_2 layers closely resembling Cu^{2+} (d^9) in cuprates[13-16].

More recently, signatures of superconductivity have also been observed in the Ruddlesden-Popper (RP) bilayer perovskite $La_3Ni_2O_7$ under high pressure, achieving a T_c of approximately 80 K above 14 GPa (ref. 17). Subsequent studies have observed zero resistance under improved hydrostatic pressure conditions facilitated by a liquid pressure-transmitting medium[18-20]. Unlike "infinite-layer" nickelates and cuprates with a d^9 electron configuration, $La_3Ni_2O_7$ hosts a bilayer NiO_2 square structure featuring $Ni^{2.5+}$ ($d^{7.5}$) ions[17]. Furthermore, the *p*-orbital of apical oxygen, which connects adjacent NiO_2 layers, couples the two nearest-neighbor $3d_{z^2}$ orbitals, suggesting that interlayer coupling may also play a crucial role in $La_3Ni_2O_7$[17]. However, in contrast to cuprate and iron-based superconductors, where superconductivity typically arises from the suppression of static long-range magnetic order in their parent phases[2-4,21], infinite-layer and bilayer $La_3Ni_2O_7$ nickelates have shown either a lack of magnetic order or hinted at the presence of weak magnetism[13,17,22,23]. This raises a fundamental question about whether magnetism plays the same crucial role in making nickelates into high-temperature superconductors.

Of particular interest, it is well known that the T_c in cuprates depends on the number of CuO_2 layers (n) in a non-monotonic way, reaching a maximum for $n = 3$ in most cases[24-26]. As a result, trilayer cuprates have the highest T_c among all cuprates, reaching up to 135 K at ambient pressure and 164 K under high pressure for mercury-based compounds[27,28]. The mechanism for this layer dependence of superconductivity remains a subject of intense and ongoing debate[26-30]. This engenders an intriguing question: can trilayer nickelates exhibit superconductivity, and if so, how might it influence T_c.

Theoretical considerations have suggested that trilayer $La_4Ni_3O_8$, with its $Ni^{1.33+}$ ($d^{8.67}$) configuration, closely parallels the cuprates with Cu^{2+}/Cu^{3+} configurations and thus stands as an ideal candidate for a high-T_c superconductor[31,32]. However, experimental investigations have thus far failed to observe superconductivity in trilayer $La_4Ni_3O_8$, both under ambient conditions and at high pressure[11,33].

In contrast to many nickelates that display insulating behavior, including trilayer $La_4Ni_3O_8$, the trilayer RP compound $La_4Ni_3O_{10}$ stands out as a rare oxide compound that maintains its metallic character even at low temperatures under ambient pressure[34,35]. Trilayer nickelate $La_4Ni_3O_{10}$ exhibits a static long-range incommensurate magnetic order accompanied by a charge order[36]. The nominal valence state of trilayer $La_4Ni_3O_{10}$ is $Ni^{2.67+}$ ($d^{7.33}$), which is different from the d^9 state typically observed in infinite-layer nickelates and cuprates or the $d^{7.5}$ state found in bilayer $La_3Ni_2O_7$. Nevertheless, the band structure of $La_4Ni_3O_{10}$ unveils intriguing features: the $d_{x^2-y^2}$

hole band bears a striking resemblance to the behavior observed in hole-doped cuprates, while the d_{z^2} band is rather flat and exhibits a 20 meV density wave-like gap opening associated with the spin order transition[35,36], reminiscent of phenomena observed in iron-based superconductors[21,37]. This distinctive combination of characteristics, coupled with its trilayer structure, positions $La_4Ni_3O_{10}$ as an ideal platform for the exploration of the interplay between magnetism, interlayer coupling, and potential superconductivity. However, the investigations of $La_4Ni_3O_{10}$ were significantly hampered by the scarcity of high-quality single crystals, which necessitated their growth under a high oxygen pressure atmosphere[34].

In this paper, we report detailed measurements of $La_4Ni_3O_{10}$ single crystals under both ambient conditions and high pressures, reaching up to 70 GPa. The high-quality $La_4Ni_3O_{10}$ single crystals were grown using a high-pressure vertical optical-image floating-zone furnace. Our X-ray diffraction (XRD) experiments conducted on powdered $La_4Ni_3O_{10}$ single crystals at ambient conditions confirm the presence of a pure phase of trilayer $La_4Ni_3O_{10}$ (Extended Data Figure 1). Through Rietveld refinement analysis, we determined that the crystal structure aligns with the $P2_1/a$ space group (Fig. 1e), consistent with previous reports[34]. Fig. 1b presents atomic-resolution high-angle annular dark-field (HAADF) images that unveil the precise atom positions, in alignment with the findings from XRD refinements. The HAADF images in large area overviews further confirm the phase purity and exceptional quality of our crystals (Extended Data Figure 6). Analysis of the chemical composition via atomic resolution EDX measurements and Z-contrast HAADF imaging on the single crystal demonstrates precise stoichiometry of La and Ni in $La_4Ni_3O_{10}$.

To assess the influence of pressure on the crystal structure, we conducted lab-based XRD measurements on powdered single crystals subjected to varying pressure conditions, reaching up to approximately 70 GPa (Extended Data Figure 2). Our analysis revealed no evidence of a pronounced structural phase transition. To gain further insights into the possibility of a subtle structural transition, we conducted synchrotron-based XRD measurements with improved resolution (Extended Data Figure 3). It is shown that the diffraction peaks within the range of $12.5°<2\theta<14°$ exhibit a noticeable evolution with increasing pressure, indicative of a structural phase transition. The refinement analyses reveal a subtle structural transition associated with the tilting of the NiO_6 octahedra, shifting from monoclinic $P2_1/a$ to tetragonal $I4/mmm$ at pressures exceeding approximately 15.4 GPa (Extended Data Figure 3). Concurrently, the Ni–O–Ni angle between adjacent NiO_2 layers undergoes a change from around 166° to 180° during this phase transition (Fig. 1e, 1f), potentially enhancing interlayer coupling. The lattice constants and cell volume also exhibited progressive suppression under pressure, with an anomaly observed near the structural phase transition (Fig. 1c, 1d).

To further characterize the material, magnetic susceptibility measurements were conducted, revealing a distinct kink in the data at $T_N \approx 136$ K (Fig. 2a), suggesting the emergence of the long-range spin and charge order, as previously revealed through neutron diffraction experiments[36]. This phase transition was corroborated by heat capacity measurements, which exhibited a pronounced peak at a similar temperature (Fig. 2c).

The electrical resistance $R(T)$ of $La_4Ni_3O_{10}$ single crystals under various pressure

conditions is presented in Fig. 2b and Fig. 3a-e. At ambient pressure, $La_4Ni_3O_{10}$ displays a characteristic metallic behavior, with $R(T)$ exhibiting a decrease as the temperature descends below 300 K. A distinctive, steplike kink in the resistivity curve manifests at the spin/charge ordering temperature T_N (Fig. 2b). It's worth emphasizing that the spin/charge order phase transition observed in our measurements displays an exceptional sharpness, which is notable in comparison to previous studies. This indicates the high quality of our $La_4Ni_3O_{10}$ single crystals, setting the stage for precise investigations into its physical properties under pressure.

When external pressure is exerted on the piston-cylinder cell, the characteristic kink related to the spin/charge ordering in the resistance curve is rapidly suppressed (Fig. 3a), which is consistent with previous measurements on a powder sample below 1.28 GPa[38]. The spin ordering transition temperature T_N also shifts towards lower temperatures and reaches 122 K at 2.5 GPa (Fig. 3a).

Resistances above 2.5 GPa were measured in a Be-Cu alloy diamond anvil cell (DAC). To ensure the best hydrostatic condition inside the DAC, we use helium as the pressure-transmitting medium. The resistance initially exhibits weak insulating behavior at 3.0 GPa (Fig. 3b). As pressure increases, metallic behavior is restored at high temperatures. This metallic behavior is subsequently followed by an upturn in resistance as temperatures decrease, which is then succeeded by a sharp drop in resistance below a critical temperature T_c of 4.5 K at 15.5 GPa (see Fig. 3b). With further increments in pressure, T_c continues to rise, ultimately reaching a point where zero resistance is observed at pressures exceeding 43 GPa (Fig. 3b-d). This compellingly signifies the emergence of superconductivity, with the onset superconducting transition temperature

ranging from 4.5 K to around 30 K.

We also conducted temperature-dependent resistance measurements in a DAC using KBr as the pressure-transmitting medium. Across the pressure range spanning from 2.2 to 24.6 GPa, a moderate decrease of resistance below a critical temperature of 2-20 K is observed (Fig. 3e). This together with the weak upturn in resistance in the normal state, suggests a relatively limited superconducting volume within this pressure range. As the pressure is raised further, a significant sharp reduction in resistance becomes evident at approximately 15-30 K, observed at pressures of 38.0 GPa and beyond (Fig. 3e) and the onset T_c reaches 30.1 K at 69.0 GPa (Fig. 3e, Extended Data Figure 5). However, small residue resistance below T_c was observed in this configuration, likely attributed to the less hydrostatic conditions resulting from the pressure-transmitting medium KBr.

To provide additional confirmation of the pressure-induced superconductivity, we conducted ultrasensitive DC magnetic susceptibility measurements under high pressures within a custom-built miniature Be-Cu alloy DAC, using liquid nitrogen as the pressure-transmitting medium to provide a hydrostatic pressure environment. A distinctive diamagnetic response at T_c is clearly evident in the zero-field-cooled (ZFC) curve, and as pressure increases, T_c also rises, further confirming the emergence of superconductivity (Fig. 3f-i). The difference of susceptibilities between ZFC and field cooled (FC) curves in the normal states is due to the magnetic background of the pressure cell with residual paramagnetic impurities.

Interestingly, concomitant with the emergence of zero resistance at 43 GPa, the normal

state resistance follows a linear temperature dependence up to 300 K (Fig. 3b). This behavior is a hallmark of the so-called "strange metal" state, a characteristic phenomenon observed in optimal doped cuprates, certain iron-based materials and nickelate superconductors [2,17,19,39-43], implying the existence of strong correlations and underscores the unconventional nature of superconductivity. Similar strange metal behavior was also confirmed in the measurements conducted within the KBr DAC above 38.0 GPa (Fig. 3e).

Figs. 4a-d display the temperature-dependent magnetoresistance measured in magnetic fields perpendicular to the *ab* plane under various pressures. As the magnetic field is increased, superconductivity is progressively suppressed, providing further confirmation that the transition in resistance is due to the onset of superconductivity. We use the 90% resistance transition to the normal state near T_c and fit it to the Ginzburg-Landau form $H_{c2}(T) = H_{c2}(0)[(1–t^2)/(1+t^2)]$, where $t = T/T_c$. This analysis yields an estimation of the upper critical field, with values reaching 44 T at 63.0 GPa when utilizing the helium DAC, and 48 T at 69.0 GPa with the KBr DAC (Fig. 4e, Extended Data Figure 5). These values are comparable with the upper critical fields observed in cuprate superconductors exhibiting similar T_c values[44]. Additionally, our estimation of the in-plane superconducting coherence length approximates to 26 Å at 69.0 GPa.

Figure 1a summarizes the pressure dependent spin/charge order and superconductivity phase diagram in trilayer $La_4Ni_3O_{10}$. This phase diagram bears some analogy to those found in cuprate and iron-based superconductors[2,21], where high-temperature superconductivity arises upon suppression of a long-range magnetic order. From the

electronic structure perspective, it suggests that the d_{z^2} band could play an important role in shaping the pressure-dependent phase diagram of $La_4Ni_3O_{10}$. The d_{z^2} band is notably flat and displays a 20 meV spin density wave-like gap[35]. This unique electronic structure feature, coupled with its propensity to interact with the *p*-orbital of apical oxygen, renders the d_{z^2} band highly susceptible to external pressure, with the potential to alter nesting conditions and influence the spin/charge density wave order.

Therefore, the concurrent emergence of a sharp superconducting transition and strange metal behavior could be attributed to the pressure effect that suppresses the density wave gap, brings the flat d_{z^2} band into proximity with the Fermi surface, consequently inducing strong correlations and fostering the emergence of the "strange metal" behavior. Simultaneously, the closing of the density wave gap dampens the static spin-density wave order and promotes dynamic spin fluctuations, paving the way for superconductivity to emerge, where the hole Fermi surface associated with the $d_{x^2-y^2}$ orbital may also come into play.

If this analysis were extended to the bilayer system, it suggests that the absence of (or weak) static magnetic order in $La_3Ni_2O_7$ may be attributed to the fact that the d_{z^2} band lies considerably further below the Fermi level compared to $La_4Ni_3O_{10}$[35,45]. However, even the flat bands located away from the Fermi level have the potential to generate high-energy spin fluctuations, which could exert a noteworthy influence on the phase diagram or serve as a mediator of electron pairing[46]. Further investigations in this direction are warranted to fully elucidate the role of magnetism in nickelate superconductors.

Furthermore, it's important to consider the impact of the interlayer coupling, a factor that could potentially promote superconductivity and has been intensively discussed in multilayer cuprates and bilayer $La_3Ni_2O_7$[2,17,29,30,47]. The observation of pressure induced superconductivity accompanied by a structural transition from monoclinic to tetragonal phases also suggests a potential significant role of interlayer coupling in trilayer $La_4Ni_3O_{10}$. However, unlike cuprate superconductors where the highest T_c is achieved in trilayer systems, in the case of trilayer $La_4Ni_3O_{10}$, the T_c is lower than that of bilayer $La_3Ni_2O_7$. This discrepancy suggests the presence of distinct interlayer interaction mechanisms between these two systems. Additional investigations are needed to elucidate these coupling mechanisms, particularly focusing on differences in carrier concentrations between the inner and outer NiO_2 layers, as well as the interlayer coupling between the two outer NiO_2 layers. These factors are crucial for understanding the evolution of T_c in multilayer superconductors[2,29,30,47].

In summary, we present signatures of pressure induced superconductivity in trilayer nickelate $La_4Ni_3O_{10}$ single crystals. Our experiments also unveil intriguing "strange metal" behavior in the normal state, characterized by linear temperature dependence of resistance up to 300 K, which may be linked to the enhanced spin fluctuations and strong correlations induced by the flat d_{z^2} band positioned near the Fermi level. Furthermore, the layer-dependent T_c in nickelates is distinct from that observed in cuprates, suggesting unique interlayer coupling and charge transfer mechanisms specific to nickelates. Further research is required to fully understand the precise role of interlayer coupling in the pairing, especially considering the differences in carrier concentrations between the inner and outer NiO_2 layers, as well as the interlayer

coupling between the two outer NiO_2 layers, which are absent in the bilayer system. Additionally, a comprehensive exploration of the role of the $d_{x^2-y^2}$ orbital and pairing symmetry is necessary for a complete understanding. In essence, our findings establish a promising new material platform, inviting deeper exploration into the intricate interplay between spin/charge order, flat band structure, interlayer coupling, strange metal behavior and high-temperature superconductivity. This avenue of research holds great potential for uncovering novel phenomena and advancing our understanding of high-temperature superconductors.

Note added:

While preparing this manuscript, we became aware of three related preprints that reported resistance measurements on $La_4Ni_3O_{10}$ polycrystalline samples[48-50]. References 49 and 50 describe a reduction in resistance—ranging from 4-7% below the 15-20 K temperature range—under pressures exceeding roughly 30 GPa, while ref. 48 does not observe this phenomenon below 50 GPa.

Methods

Growth and characterization of $La_4Ni_3O_{10}$ single crystals

The precursor powder for the $La_4Ni_3O_{10}$ compound was prepared using the conventional solid-state reaction method. Chemically stoichiometric raw materials, La_2O_3 and NiO (Aladdin, 99.99%), were meticulously ground and mixed using a Vibratory Micro Mill (FRITSCH PULVERISETTE 0). An additional 0.5% of NiO was included to compensate for potential NiO volatilization during the crystal growth process. The resulting mixture underwent calcination at 1373 K for 24 hours, with two repeated calcination cycles to ensure complete and homogeneous reactions.

Subsequently, the resulting precursor material was pressed into a cylindrical rod, approximately 13 cm in length and 6 mm in diameter, using a hydrostatic pressure of 300 MPa. The shaped rod then underwent once sintering at 1673 K for 12 hours in air. Single crystals were grown using a vertical optical-image floating zone furnace (Model HKZ, SciDre GmbH, Dresden) at Fudan University. During the crystal growth process, we carefully maintained an oxygen pressure within the range of 18-22 bar, and employed a 5 kW Xenon arc lamp as the light source. The rod was rapidly traversed through the growth zone at a speed of 15 mm/h to enhance the density, after which a growth rate of 3 mm/h was maintained.

The STEM experiments were performed on a double aberration corrected S/TEM (Themis Z, Thermo Fisher Scientific) operated at 300 kV. For STEM-HAADF imaging, the probe semi-convergent angle is 21.4 mrad, and the HAADF collection angle is from 79 to 200 mrad. The atomic resolution EDX imaging was recorded with a Super-X detector.

Resistance, magnetic susceptibility and XRD measurements under high pressure

We conducted electrical resistance measurements on $La_4Ni_3O_{10}$ single crystals under pressure by using the standard van der Pauw four-probe method in a physical property measurement system (PPMS) by Quantum Design. The temperature range covered was from 1.8 to 300 K, and magnetic fields up to 9 T were applied. The electrical resistance measurements at low pressures (below 2.5 GPa) were performed using a piston cylinder cell (Fig. 3a). The pressure-transmitting medium employed in this setup was Daphne 7373. The electrical resistance measurements at high pressures (above 2.2 GPa) were performed in a diamond anvil cell with 200-300 μm culets (Fig. 3b-d, Fig. 4, Extended Data Figure 4). The sample chamber was constructed using a mixture of cubic boron

nitride and epoxy, with a diameter ranging from 140 to 280 μm. The single crystal was loaded under helium as the pressure-transmitting medium. Alternately, KBr powders were also used as a different pressure-transmitting medium (Fig. 3e, Extended Data Figure 5). Pressure calibration was carried out using ruby fluorescence peak shift at room temperature.

Ultrasensitive magnetic susceptibility measurements under pressure were conducted using a custom-built beryllium-copper alloy mini-DAC equipped with a rhenium gasket, employing a design similar to refs. 51 and 52. The mini- DAC boasts dimensions of approximately 8.5 mm in diameter and 30 mm in length. The measurements were performed using a Magnetic Property Measurement System (MPMS3, Quantum Design). The DAC includes a pair of diamond anvils with a diameter of 300 μm and a sample chamber with a diameter of 210 μm. The sample chamber was filled with single crystal of $La_4Ni_3O_{10}$ and liquid nitrogen as the pressure transmitting medium to provide a hydrostatic pressure environment. The samples had a diameter of approximately 150-200 μm and a thickness of roughly 25 μm.

In-situ lab-based high-pressure XRD measurements were carried out on powdered single crystals using a Bruker D8 Venture diffractometer, utilizing Mo Kα radiation (λ = 0.7107 Å) in a diamond anvil cell with 300-μm-diameter culets. In this configuration, we captured two-dimensional patterns of powder diffraction rings, which were subsequently processed to yield one-dimensional profiles (Extended Data Figure 2). We included a small ruby ball within the chamber to facilitate pressure calibration by monitoring the ruby's fluorescence peak shift. *In-situ* synchrotron-based high-pressure XRD measurements were performed at the beamline 15U1 at Shanghai Synchrotron Radiation Facility, China. A symmetric DAC with anvil culet sizes of 200 μm, and rhenium gaskets were used. Mineral oil was used as the pressure-transmitting medium,

and pressure was calibrated by the equation of state of Au.

† These authors contribute equally to this work.

* Correspondence and requests for materials should be addressed to J.Z. (zhaoj@fudan.edu.cn) or J.G.G. (jgguo@iphy.ac.cn) or Q.S.Z.(zengqs@hpstar.ac.cn)

References

1. Bednorz, J. G. & Müller, K. A. Possible high T_c superconductivity in the Ba–La–Cu–O system. *Z. Phys. B Condens. Matter* **64**, 189–193 (1986).

2. Lee, Patrick A., Nagaosa, N. & Wen, X. G. Doping a Mott insulator: Physics of high-temperature superconductivity. *Rev. Mod. Phys.* **78**, 17 (2006).

3. Scalapino, D. J. A common thread: The pairing interaction for unconventional superconductors. *Rev. Mod. Phys.* **84**, 1383 (2012).

4. Kamihara, Y., Watanabe, T., Hirano, M. & Hosono, H. Iron-based layered superconductor La[$O_{1-x}F_x$]FeAs(x = 0.05−0.12) with T_c = 26 K. *J. Am. Chem. Soc.* **130**, 3296−3297 (2008).

5. Maeno, Y. et al. Superconductivity in a layered perovskite without copper. *Nature* **372**, 532 (1994).

6. Wang, F. & Senthil, T. Twisted hubbard model for Sr_2IrO_4: magnetism and possible high temperature superconductivity. *Phys. Rev. Lett.* **106**, 136402 (2011).

7. Kim, Y. K., Sung, N. H., Denlinger, J. D. & Kim, B. J. Observation of a d-wave gap in electron-doped Sr_2IrO_4. *Nat. Phys.* **12**, 37−41 (2016).

8. Anisimov, V. I., Bukhvalov, D. & Rice, T. M. Electronic structure of possible nickelate analogs to the cuprates. *Phys. Rev. B* **59**, 7901–7906 (1999).

9. Lee, K.-W. & Pickett, W. E. Infnite-layer $LaNiO_2$: Ni^{1+} is not Cu^{2+}. *Phys. Rev. B* **70**, 165109 (2004).

10. Chaloupka, J. & Khaliullin, G. Orbital order and possible superconductivity in $LaNiO_3$/$LaMO_3$ superlattices. *Phys. Rev. Lett.* **100**, 016404 (2008).

11. Zhang, J. et al. Stacked charge stripes in the quasi-2D trilayer nickelate $La_4Ni_3O_8$. *Proc. Natl Acad. Sci. USA* **113**, 8945–8950 (2016).

12. Lechermann, F. Late transition metal oxides with infinite-layer structure: Nickelates versus cuprates. *Phys. Rev. B* **101**, 081110 (2020).

13. Li, D. et al. Superconductivity in an infinite-layer nickelate. *Nature* **572**, 624-627 (2019).

14. Zeng, S. et al. Phase diagram and superconducting dome of infinite-layer $Nd_{1-x}Sr_xNiO_2$ thin films. *Phys. Rev. Lett.* **125**, 147003 (2020).

15. Pan, G. A. et al. Superconductivity in a quintuple-layer square-planar nickelate. *Nat. Mater.* **21**, 160–164 (2022).

16. Ding, X. et al. Critical role of hydrogen for superconductivity in nickelates. *Nature* **615**, 50-55 (2023).

17. Sun, H. et al. Signatures of superconductivity near 80 K in a nickelate under high pressure. *Nature* **621**, 493-498 (2023).

18. Hou, J. et al. Emergence of high-temperature superconducting phase in the pressurized $La_3Ni_2O_7$ crystals. arXiv:2307.09865 (2023).

19. Zhang, Y. et al. High-temperature superconductivity with zero-resistance and strange metal behaviour in $La_3Ni_2O_7$. arXiv:2307.14819 (2023).

20. Wang, G. et al. Pressure-induced superconductivity in polycrystalline $La_3Ni_2O_{7-x}$ arXiv:2309.17378 (2023).

21. Dai, P. Antiferromagnetic order and spin dynamics in iron-based superconductors. *Rev. Mod. Phys.* **87**, 855-893 (2015).

22. Ling, C. D. et al. Neutron diffraction study of $La_3Ni_2O_7$: structural relationships among n = 1, 2, and 3 phases $La_{n+1}Ni_nO_{3n+1}$. *J. Solid State Chem.* **152**, 517–525 (1999).

23. Gu, Y. et al. Effective model and pairing tendency in bilayer Ni-based superconductor $La_3Ni_2O_7$. arXiv:2306.07275 (2023).

24. Scott, B. A. et al. Layer dependence of the superconducting transition temperature of $HgBa_2Ca_{n-1}Cu_nO_{2n+2+\delta}$. *Physica C* **230**, 239–245 (1994).

25. Kuzemskaya, I. G., Kuzemsky, A. L. & Cheglokov, A. A. Superconducting properties of the family of mercurocuprates and role of layered structure. *J. Low-Temp. Phys.* **118**, 147–152 (2000).

26. Iyo, A. et al. T_c vs n Relationship for Multilayered High-T_c Superconductors. *J. Phys. Soc. Jpn.* **76**, 094711 (2007).

27. Schilling, A., Cantoni, M., Guo, J. D. & Ott, H. R. Superconductivity above 130 K in the Hg–Ba–Ca–Cu–O system. *Nature* **363**, 56–58 (1993).

28. Gao, L. et al. Superconductivity up to 164 K in $HgBa_2Ca_{m-1}Cu_mO_{2m+2+\delta}$ (m = 1, 2, and 3) under quasihydrostatic pressures. *Phys. Rev. B* **50**, 4260(R) (1994).

29. Chakravarty, S., Kee, H.-Y. & Volker, K. An explanation for a universality of transition temperatures in families of copper oxide superconductors. *Nature* **428**, 53–55 (2004).

30. Berg, E., Orgad, D. & Kivelson, Steven A. Route to high-temperature superconductivity in composite systems. *Phys. Rev. B* **78**, 094509 (2008).

31. Botana, A. S. Pardo, V. & Norman, M. R. Electron doped layered nickelates: Spanning the phase diagram of the cuprates. *Phys. Rev. Materials* **1**, 021801(R) (2017).

32. Nica, E. M. et al. Theoretical investigation of superconductivity in trilayer square-planar nickelates. *Phys. Rev. B* **102**, 020504(R) (2020).

33. Cheng, J. G. et al. Pressure Effect on the Structural Transition and Suppression of the High-Spin State in the Triple-Layer *T'*-$La_4Ni_3O_8$. *Phys. Rev. Lett.* **108**, 236403 (2012).

34. Zhang, J. et al. High oxygen pressure floating zone growth and crystal structure of the metallic nickelates $R_4Ni_3O_{10}$ (*R* = La, Pr). *Phys. Rev. Materials* **4**, 083402 (2020).

35. Li, H. et al. Fermiology and electron dynamics of trilayer nickelate $La_4Ni_3O_{10}$. *Nat. Commun.* **8**, 704 (2017).

36. Zhang, J. et al. Intertwined density waves in a metallic nickelate. *Nat. Commun.* **11**, 6003 (2020).

37. Hu, W. Z. et al. Origin of the Spin Density Wave Instability in AFe_2As_2(A = Ba,Sr) as Revealed by Optical Spectroscopy. *Phys. Rev. Lett.* **101**, 257005 (2008).

38. Wu, G., Neumeier, J. J. & Hundley, M. F. Magnetic susceptibility, heat capacity, and pressure dependence of the electrical resistivity of $La_3Ni_2O_7$ and $La_4Ni_3O_8$. *Phys. Rev. B* **63**, 245120 (2001).

39. Gurvitch, M., & Fiory, A. T. Resistivity of $La_{1.825}Sr_{0.175}CuO_4$ and $YBa_2Cu_3O_7$ to 1100 K: Absence of saturation and its implications. *Phys. Rev. Lett.* **59**, 1337 (1987).

40. Kasahara, S. et al. Evolution from non-Fermi- to Fermi-liquid transport via isovalent doping in $BaFe_2(As_{41-x}P_x)_2$ superconductors. *Phys. Rev. B* **81**, 184519 (2010).

41. Yuan, J. et al. Scaling of the strange-metal scattering in unconventional superconductors. *Nature* **602**, 431–436 (2022).

42. Jiang, X. et al. Interplay between superconductivity and the strange-metal state in FeSe. *Nat. Phys.* **19**, 365–371 (2023).

43. Lee, K. et al. Linear-in-temperature resistivity for optimally superconducting (Nd,Sr)NiO_2. *Nature* 619, 288–292 (2023).

44. Grissonnanche, G. et al. Direct measurement of the upper critical field in cuprate superconductors. *Nat. Commun.* **5**, 3280 (2014).

45. Yang, J. et al. Orbital-Dependent Electron Correlation in Double-Layer Nickelate $La_3Ni_2O_7$. arXiv:2309.01148 (2023).

46. Wang, F. et al. The electron pairing of $K_xFe_{2-y}Se_2$. *Europhys. Lett.* **93**, 57003 (2011).

47. Luo, X. et al. Electronic origin of high superconducting critical temperature in trilayer cuprates. *Nat. Phys.* **19**, 1841−1847 (2023).

48. Zhang, M. et al. Effects of pressure and doping on Ruddlesden-Popper phases $La_{n+1}Ni_nO_{3n+1}$. *J. Mater. Sci. Technol.* **185**, 147-154 (2024).

49. Sakakibara, H. et al. Theoretical analysis on the possibility of superconductivity in a trilayer Ruddlesden-Popper nickelate $La_4Ni_3O_{10}$ under pressure and its experimental examination: comparison with $La_3Ni_2O_7$. arXiv:2309.09462 (2023).

50. Li, Q et al. Signature of superconductivity in pressurized $La_4Ni_3O_{10}$. arXiv:2311.05453 (2023).

51. Drozdov, A. et al. Conventional superconductivity at 203 kelvin at high pressures in the sulfur hydride system. *Nature* **525**, 73 – 76 (2015).

52. Deng, X. et al. Parvalbumin interneuron in the ventral hippocampus functions as a discriminator in social memory. *Proc. Natl. Acad. Sci. USA* **116**, 16583-16592 (2019).

Acknowledgments This work was supported by the Key Program of the National Natural Science Foundation of China (Grant No. 12234006), the National Key R&D Program of China (Grant No. 2022YFA1403202), the Beijing Natural Science Foundation (Grant No. Z200005), and the Shanghai Municipal Science and Technology Major Project (Grant No. 2019SHZDZX01). Y.H.Z. was supported by the Youth Foundation of the National Natural Science Foundation of China (Grant No. 12304173). H.L.W. was supported by the Youth Foundation of the National Natural Science Foundation of China (Grant No. 12204108). B.Y.P. was supported by the Natural Science Foundation of Shandong Province (Grant No. ZR2020YQ03). D.P and Q.S.Z. acknowledge the financial support from the Shanghai Science and Technology Committee (No. 22JC1410300) and Shanghai Key Laboratory of Material Frontiers Research in Extreme Environments (No. 22dz2260800). A portion of this work was carried out at the Synergetic Extreme Condition User Facility (SECUF).

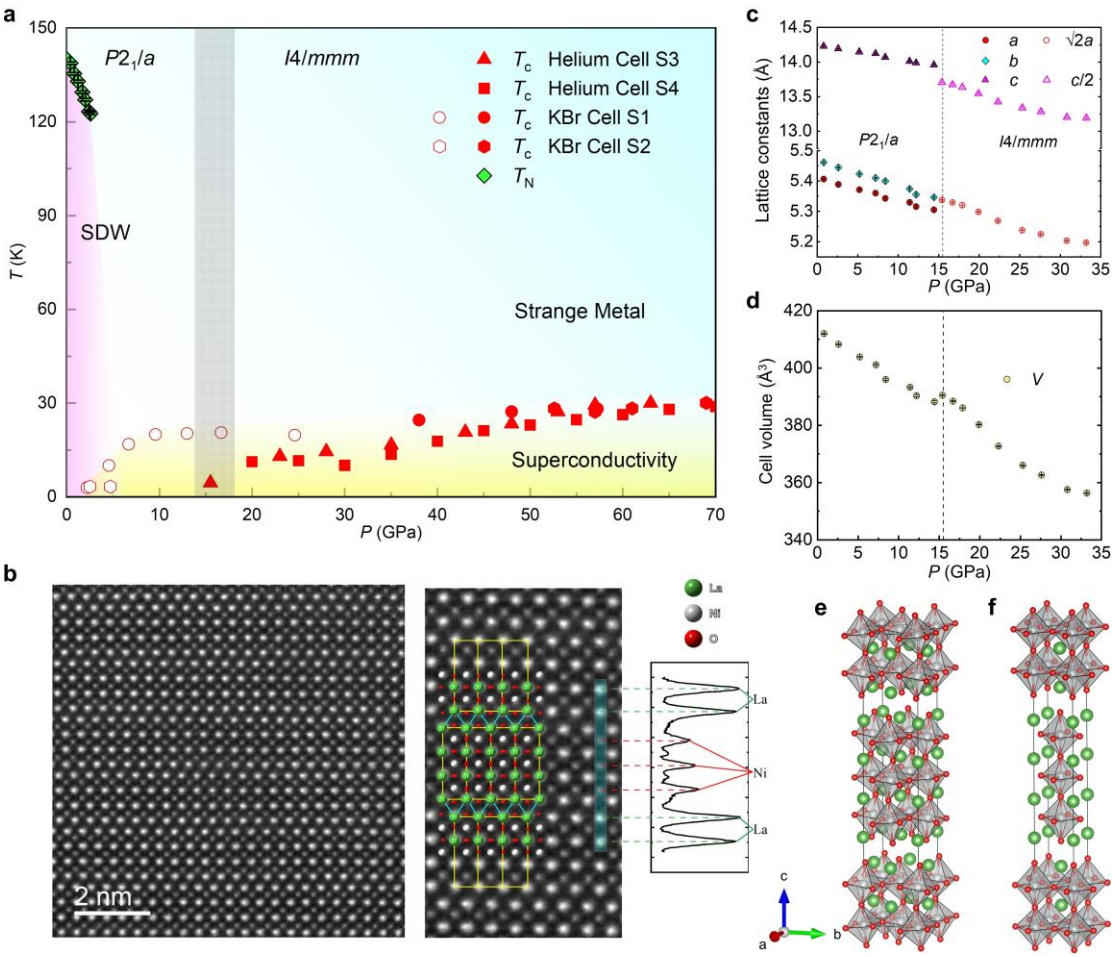

Figure 1 | Pressure-dependent lattice structure and phase diagram of $La_4Ni_3O_{10}$. **a,** Phase diagram of $La_4Ni_3O_{10}$ under pressure. The red solid triangles and squares represent T_c (onset) of sample 3 (S3) and sample 4 (S4) in the helium DAC, respectively. The T_c (onset) is defined as the temperature below which the resistance deviates from its linear dependence at high temperature. The red solid circles and hexagons represent the T_c (onset) at pressures above 38 GPa of sample 1 (S1) and sample 2 (S2), respectively, where a pronounced sharp drop in resistance below T_c is evident in the KBr DAC. The red open circles denote the T_c (onset) at pressures below 25 GPa in the KBr DAC, where a moderate decrease in resistance below T_c is observed (Fig. 3e). The green diamonds denote the T_N determined from resistance measurements in Fig. 3a. Shaded area highlights the region of the structural transition. **b**, Atomic-resolution high-angle annular dark-field images along the [110] direction at ambient pressure, featuring three layers of NiO_2 separated by LaO spacers. **c**, Lattice constants *a*, *b*, *c* extracted from the synchrotron-based XRD patterns at various pressures at room temperature (Extended Data Figure 3). **d,** Cell volume *V*. A subtle structural transition from monoclinic $P2_1/a$ to tetragonal *I*4/*mmm* at a pressure of approximately 15.4 GPa is observed. **e**, Crystal structure of $La_4Ni_3O_{10}$ at ambient pressure with a monoclinic $P2_1/a$ structure. **f**, Crystal structure of $La_4Ni_3O_{10}$ at 20 GPa with a tetragonal *I*4/*mmm* structure.

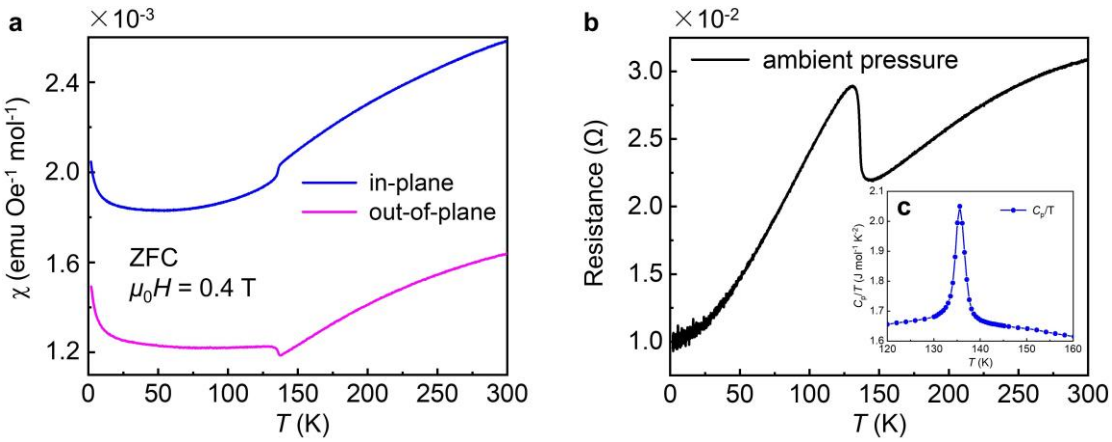

Figure 2 | Magnetic susceptibility, resistance and specific heat of $La_4Ni_3O_{10}$ single crystal at ambient pressure. **a,** Magnetic susceptibility of $La_4Ni_3O_{10}$ measured from 2 to 300 K with an applied field of 0.4 T, parallel and perpendicular to the *ab* plane. The SDW/CDW transition characterized by a kink in the $\chi(T)$ curve occurs at $T_N \approx 136$ K. **b,** Resistance of $La_4Ni_3O_{10}$ in the *ab* plane at ambient pressure. **c,** Specific heat of $La_4Ni_3O_{10}$ near T_N.

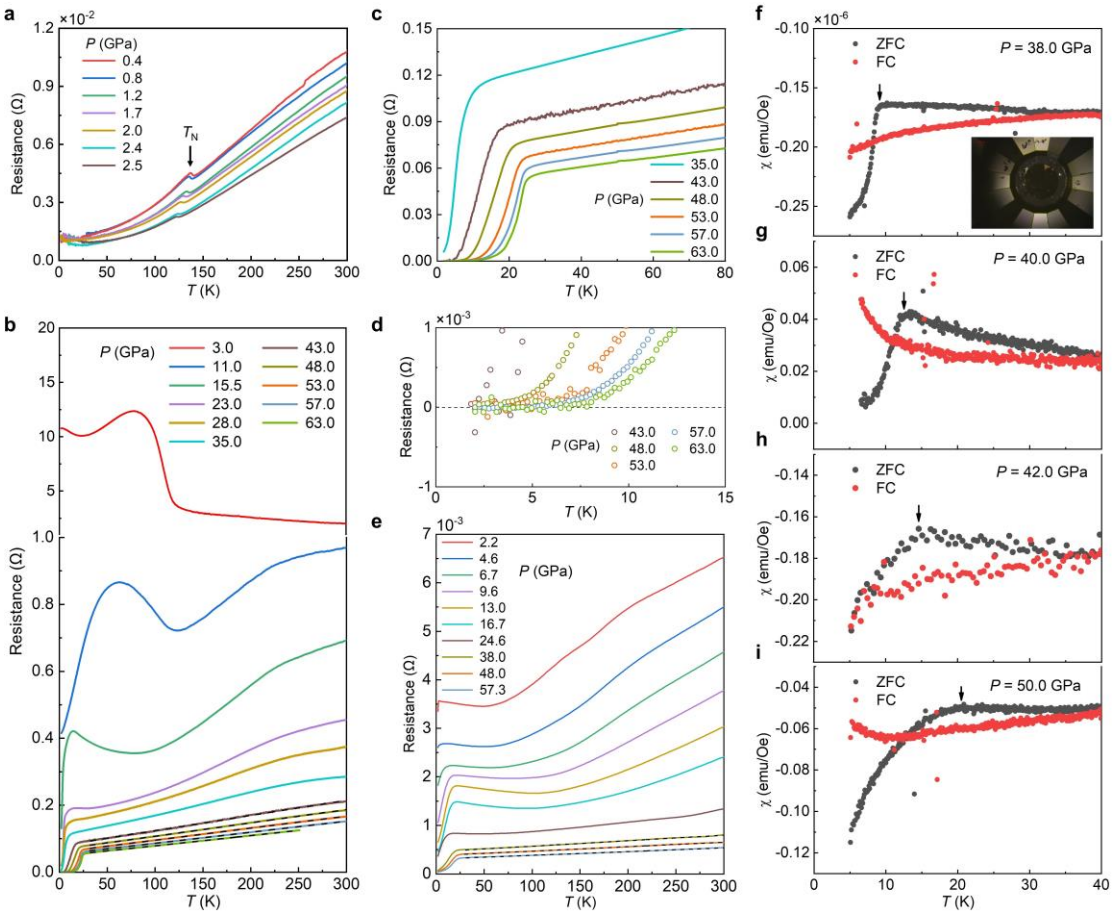

Figure 3 | Temperature-dependendent resistances and susceptibilities of $La_4Ni_3O_{10}$ single crystals under various pressures. **a,** Resistances at pressures spanning 0.4 to 2.5 GPa in the piston cylinder cell. The SDW/CDW transition at T_N is progressively suppressed with increasing pressure. **b**, Resistances at pressures ranging from 3.0 to 63.0 GPa in the helium DAC. The diamond broke upon warming to around 250 K at 63.0 GPa. The black dashed lines depict the linear fit of the normal state resistances. **c**, Resistances in the helium DAC near the superconducting transition. Zero resistances are observed above 43.0 GPa. **d**, An enlarged view of the resistance curve below T_c within the helium DAC, providing a clear and evident demonstration of zero resistance. **e,** Resistances at pressures ranging from 2.2 to 57.3 GPa in the KBr DAC. The black dashed lines depict the linear fit of the normal state resistances. **f**, Temperature dependent DC susceptibility of $La_4Ni_3O_{10}$ at 38.0 GPa under a magnetic field of 20 Oe applied perpendicular to the *ab* plane using the zero-field-cooled (ZFC) and field-cooled (FC) modes. A distinct superconducting diamagnetic response at T_c is clearly observed in the ZFC curve. The inset shows the photo of the crystal in the mini-DAC. **g**, Temperature-dependent DC susceptibility measured at 40.0 GPa and 10 Oe. **h**, Temperature-dependent DC susceptibility measured at 42.0 GPa and 20 Oe. **i**, Temperature-dependent DC susceptibility measured at 50.0 GPa and 10 Oe. The black arrows indicate the superconducting transition temperatures.

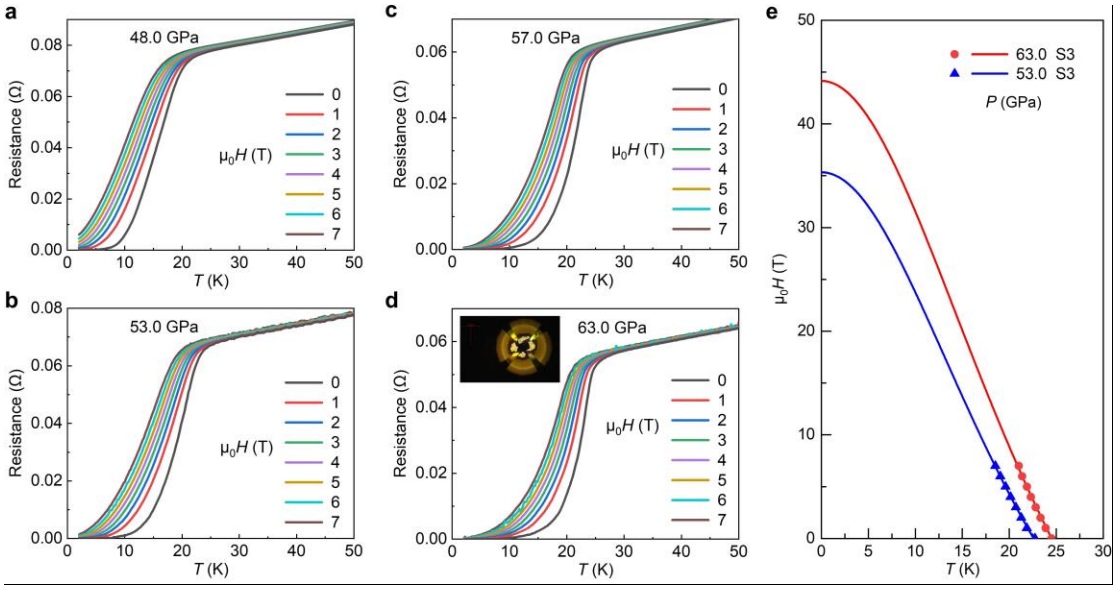

Figure 4 | Magnetic field effects on the superconducting transition in $La_4Ni_3O_{10}$. **a**, Field dependences of electrical resistance at 48.0 GPa for sample S3. **b,** 53.0 GPa. **c,** 57.0 GPa. **d**, 63.0 GPa; the inset shows a photograph of the electrodes used for high-pressure resistance measurements. **e,** The Ginzburg–Landau fittings of the upper critical fields at 53.0 and 63.0 GPa. The magnetic fields are applied perpendicular to the *ab* plane.